

Monte Carlo Simulation of CRAND Protons Trapped at Low Earth Orbits

Ritabrata Sarkar*, Abhijit Roy

Indian Centre for Space Physics, 43 Chalantika, Garia Station Road, Kolkata 700084, W.B., India

Abstract

The Cosmic Ray Albedo Neutron Decay (CRAND) is believed to be the principal mechanism for the formation of inner proton radiation belt – at least for relatively higher energy particles. We implement this mechanism in a Monte Carlo simulation procedure to calculate the trapped proton radiation at the low Earth orbits, through event-by-event interaction of the cosmic ray particles in the Earth’s atmosphere and their transportation in the magnetosphere. We consider the generation of protons from subsequent decay of the secondary neutrons from the cosmic ray interaction in the atmosphere and their transport (and/or trapping) in the geomagnetic field. We address the computational challenges for this type of calculations and develop an optimized algorithm to minimize the computation time. We consider a full 3D description of the Earth’s atmospheric and magnetic-field configurations using the latest available models. We present the spatial and phase-space distribution of the trapped protons considering the adiabatic invariants and other parameters at the low Earth orbits. We compare the simulation results with the trapped proton flux measurements made by *PAMELA* experiment at low Earth orbit and explain certain features observed by the measurement.

Keywords: Trapped protons at low Earth orbit, CRAND protons, Monte Carlo simulation, Radiation belt

*Corresponding author

Email addresses: ritabrata.s@gmail.com (Ritabrata Sarkar), aviatphysics@gmail.com (Abhijit Roy)

1. Introduction

The study of the inner radiation belt is important, as this hostile radiation environment impose crucial hazards to the satellites and space missions at low and middle Earth orbits. While, the outer radiation belt is predominantly composed of energetic electrons, the inner belt mainly consists of energetic protons up to a few GeV, with a trace of e^\pm and some other ions. The trapped protons in the radiation belt may have long residence time (up to several thousand years) and thus the accumulated radiation effect results from long time inputs from different sources like solar protons and Galactic Cosmic Rays (GCR). Several processes control the internal dynamics of the radiation belts. Radial diffusion provides the inward transport of the solar protons injected into the radiation belt at $L \gtrsim 2$, during large solar proton events and magnetic storms (Lorentzen et al., 2002; Hudson et al., 2004). Losses of radiation belt particles are imposed by the processes like: ionization of the neutral atmosphere, energy loss to the plasmasphere and ionosphere, inelastic nuclear scattering and adiabatic energy and drift shell changes due to geomagnetic secular variations. For the radiation intensity at energies $\lesssim 100$ MeV and for $L \gtrsim 1.3$ are dominated by the solar protons (Selesnick et al., 2007). Otherwise, the protons from the β -decay of the free neutrons produced by the GCR interaction with the Earth's atmosphere, according to Cosmic Ray Albedo Neutron Decay (CRAND) mechanism (Singer, 1958; Farley & Walt, 1971), dominates the radiation belt.

There are some empirical trapped proton models available, to represent the inner radiation belt, like: NASA AP8/AP9 model (Sawyer & Vette, 1976; Ginet et al., 2013), the model provided by the Institute of Nuclear Physics of Moscow State University (Getselev et al., 1991), PSB97 model (Heynderickx et al., 1999) etc. Selesnick et al. (2007) came up with a theoretical model of the inner proton radiation belt considering the physics and mechanism that populates the radiation belt. There are several satellite experiments that contributed to the understanding and modeling of the radiation belt like CRRES (Gussenhoven,

1993), SAMPEX/PET (Looper et al., 1996), TIROS/NOAA series (Huston et al., 1996) etc. Lately, measurement of CR radiation at Low Earth Orbit (LEO) by *PAMELA* mission (Picozza et al., 2007), provides important information on the high energy ($\gtrsim 70$ MeV) part of the trapped radiation at the lower region of the radiation belt.

In this work, we recreate the trapped proton distribution at LEO region, considering realistic physical models of: Earth's atmosphere, magnetosphere, GCR distribution, particle interactions in the atmosphere and their transport. We embedded all the physical mechanisms in a single Monte Carlo (MC) simulation framework. However, the total simulation procedure is segregated into different stages for convenience of the calculation and the outcome of each stage of the simulation flows into the following to get the final results. The details of the simulation procedure are discussed in Sec. 2. The spatial and spectral distribution of the secondary particles produced from the GCR interactions with the atmospheric nuclei depend on the rigidity cut-off of the GCR at different locations determined by the geomagnetic field distribution. The albedo neutrons produced in this way will have location dependency. The protons generated from the subsequent β -decay get trapped or escape according to their rigidity that depends on the energy and location of their generation. To include all these effects we perform the simulation starting right from the generation of GCR distribution at the Earth's orbit, their transportation into the Earth's atmosphere depending on their rigidity and subsequent interaction to produce secondary particles. Then, we consider the neutrons which escape into the space and decay to produce protons. The trajectories of these protons can be calculated individually from the equation of motion in the magnetic field. However, calculating the actual path due to Newton-Lorentz motion may lead to time consuming computation. So, instead, we adopted the guiding center equation to calculate the average track of the particles. In this work, we carry on with some simplified assumptions, like neglecting geomagnetic secular variation and considering an average heliospheric effect which, in principle, can limit some aspects of the calculation and will be discussed later at proper places (viz. Sec.

3.4). We concentrate on the high energy part $\gtrsim 50$ MeV to compare the simulation results with *PAMELA* measurement of trapped protons (Adriani et al., 2015).

In the following Sec. 2, we outline the general simulation procedure to describe the neutron generation from the GCR interaction with Earth's atmosphere, proton production from subsequent decay and their entrapment in the geomagnetic field. In Sec. 3, we present the analysis procedure and results from the calculations. We compare the simulation outcome with the recent measurements of the trapped protons by the *PAMELA* mission in Sec. 4. Finally we conclude the results from this work in Sec. 5.

2. Simulation Procedure

We considered an event-by-event simulation procedure using the MC technique to study the problem of trapped protons from the CRAND mechanism. The general scheme for the simulation is as follows. At first we calculate the neutron production in the atmosphere due to the interaction of the CR particles. These free neutrons, therefore decay to produce protons according to the β -decay process. Finally, the protons either get trapped into the radiation belt, transported off to the outer space or absorbed at the Earth – according to their position of generation, rigidity, the direction of motion (pitch angle) and the geomagnetic field distribution. In the following subsections we briefly discuss these steps of the simulation procedure.

2.1. Neutron production in the atmosphere

To calculate the neutron production from the CR interaction in the atmosphere, we considered a detailed MC simulation using Geant4 simulation toolkit (Agostinelli et al., 2003). The details of this simulation procedure can be found in Sarkar et al. (2020). However, for the sake of completeness we briefly mention the key aspects of the simulation here. We implemented a full 3D model of the atmosphere and magnetosphere in Geant4 simulation environment, with proper

distribution of primary GCR particles at the Earth’s orbit and using a list of interaction processes suitable for the energies and phenomena considered in the simulation.

The atmospheric matter distribution which depends on the location, time and other conditions like solar activity, is realized using the NRLMSISE-00 standard atmospheric model (Picone et al., 2002). The atmospheric distribution is limited up to 100 km from the Earth’s surface since most of the CR interactions effectively take place below this level to produce neutrons, which is our prime concern for this step of the simulation. The whole atmosphere is subdivided into 100 concentric spherical layers with the thickness equal in logarithmic scale of altitude to implement the gradual material distribution. However, with an approximation, to evade the complexity in the atmospheric geometry construction, we did not implement the zonal and meridional distribution of the atmospheric constituents in the current simulation. We neither considered the temporal variation of the model parameters. Instead, we considered global atmospheric parameters at each layer corresponding to the tropical region (23°N, 88°E) and at a fixed time in the month of May in 2016 (Sarkar et al., 2020).

The magnetic field distribution is also embedded in the simulation environment along with the atmospheric matter distribution which directly takes care of the rigidity cut-off of the charged primary particles and defines the trajectories of the primary and secondary charged particles. The inner magnetic field due to the Earth’s inherent magnetism extends up to about 4 Earth radii (R_E) from the surface and is represented by the 12th generation IGRF model (Thébault et al., 2015) with proper input parameters at moderate solar condition (during 2016 at declining phase of 24th solar cycle; vide Sarkar et al. (2020)). The external magnetic field depends on the inter-planetary magnetic field and solar conditions, is considered up to 25 R_E defined by using the Tsyganenko model (Tsyganenko & Andreeva, 2016). Here also, in defining the magnetic field model, we did not consider the temporal variation due to solar activity or the secular variation of the geomagnetic field, instead used the average field distribution corresponding to the above mentioned time.

For the primary GCR flux distribution, we considered only the most abundant components, i.e., protons (H) and helium nuclei (He) which constitute about 99% of the GCR flux. We used up-to-date spectral information of the primary CR particle flux using the model for local interstellar spectrum given by Vos & Potgieter (2015). This model is conceived by using the *Voyager I* data of the post-heliopause CR observation complimented by *PAMELA* and *AMS02* data. The details of the primary CR flux distribution is given in Sarkar et al. (2020). To maintain the efficiency of the simulation, we generated an isotropic distribution of the charged particles from a geocentric spherical surface at 500 km above the Earth’s surface and backtracked them to reach an outer surface at $25 R_E$ in presence of the magnetic field distribution. We select only those particles that reach the outer sphere as the allowed CR particle tracks at 500 km and proceed with the simulation for atmospheric interactions. Thus, we consider the modulation of the primary CR at the Earth’s orbit by the geomagnetic field surrounding Earth till $25 R_E$. We restricted the primary generation in the energy range of 0.1–800.0 GeV/n. We simulated 3.5×10^5 particles (both for H and He) that survived the rigidity cut-off at 500 km above the Earth’s surface in the back-tracking method, to interact with the atmosphere. To achieve this number of particles to interact in the atmosphere, the simulation discarded about 10^6 H and 1.5×10^6 He particles. Simulation of these number of events was required to validate simulation results with the *AMS02* observations with comparable significance (Sarkar et al., 2020).

To simulate the interaction of high energy particles with the atmosphere we used the reference physics list (QGSP physics list with Binary Cascade model *QGSP_BIC_HP*) provided in Geant4, which optimally covers the interaction processes relevant here.

Here, we are particularly interested in the neutrons produced due to CR interactions in the atmosphere, which move outwards from the atmosphere. So, we calculated the secondary neutron distribution at the spherical surface at 100 km above the Earth’s surface, which are outgoing from the atmosphere into the space (albedo neutrons). The spatial distribution of the secondary neutrons

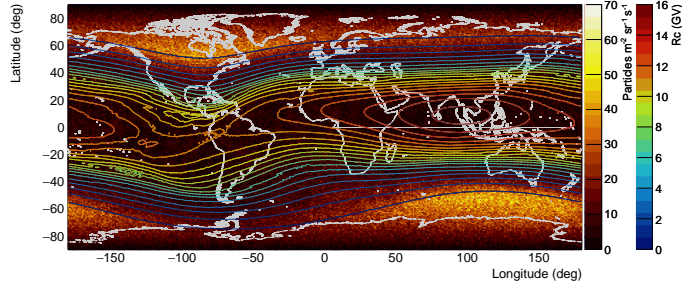


Figure 1: Positional distribution of the secondary neutron flux at the top of the atmosphere (100 km from Earth’s surface) as obtained from the simulation, due to primary cosmic rays (H and He). The contour plot of vertical rigidity cut-off values at different locations along with the continental coast line map for physical location guidance are also superimposed in the plot.

depend on the rigidity cut-off of the primary CR particles and hence on the geomagnetic field distribution. The spatial distribution (in geographic latitude (θ)/longitude (ϕ)) of the neutrons at 100 km above the Earth’s surface is shown in Fig. 1 along with vertical rigidity cut-off values at different locations. The apparent drop-off in the neutron flux toward the poles are due to the coordinate (θ - ϕ) we chose for the plotting. (For a uniform positional distribution on a spherical surface θ is not isotropic in $[0, \pi]$ rather $\cos \theta$ is uniform in $[0, 1]$.) The overlaid contour plot is also calculated according to the chosen coordinates and this note on the distortion of the plots in θ - ϕ coordinate is also valid for other subsequent plots (viz. Fig. 9 and 10). The positional distribution, as well as the directional and spectral distributions of the secondary neutrons are used to generate the CRAND protons described in the next Sec. 2.2. We used the calculated positional distribution shown in Fig. 1 to generate random neutron positions in θ/ϕ for the next step of the simulation.

The propagation (or momentum) direction of the produced neutrons are also important in this concern; since the pitch angle of the protons, generated from the decay of these neutrons, depends on their direction. We have shown this directional dependence in terms of θ_Z/ϕ_Z angle in Fig. 2. Where θ_Z is

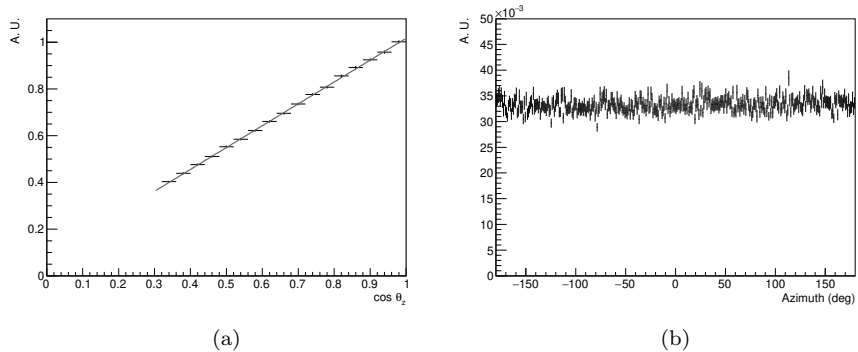


Figure 2: (a) Neutron directional distribution as a function of $\cos \theta_Z$. (b) Neutron directional distribution as a function of the azimuthal angle (ϕ_Z).

the angle between propagation direction and zenith direction at the position of the neutron and ϕ_Z is the azimuthal angle about the zenith direction and with respect to local north. The cut-off that appeared in the $\cos \theta_Z$ distribution of the albedo neutron is due to the fact that, we generated the primary H and He from a spherical surface at 500 km above the Earth's surface while the extent of the atmosphere is only up to 100 km. So, only the primaries inside a limited solid angle (about the zenith direction) among all those isotropically generated from the spherical surface, can interact with the atmosphere. While this particular configuration of the primary generation was originally considered to serve some general purpose to calculate space and atmospheric radiation due to cosmic rays as discussed in Sarkar et al. (2020), this may have some minor effect on the low pitch angle trapped particle population as will be discussed later at proper place (viz. Sec. 3.1 and 3.2).

The energy distribution of the produced neutron flux is shown in Fig. 3. This spectrum is fitted with an empirical function with three modified cut-off power-laws (at three different energy intervals) of the form:

$$\frac{dN}{dE} = \sum_{i=1}^3 A_i E_i^{-\alpha_i} \exp \left(- \left(\frac{E_i}{B_i} \right)^{\beta_i} \right), \quad (1)$$

where the energy E_i is in the ranges ($\leftarrow: 1.5 \times 10^{-2} : 2.0 \times 10^{-2} \rightarrow$) GeV.

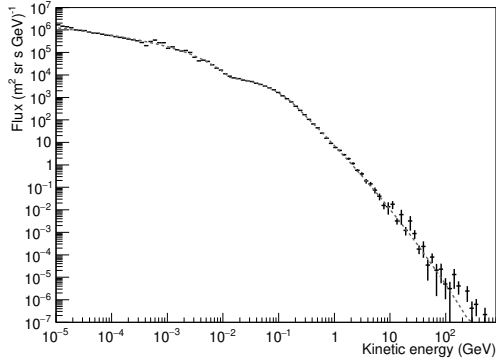


Figure 3: Albedo neutron flux distribution at the top of the atmosphere (at 100 km) due to cosmic ray (H and He) interactions in the atmosphere. The spectrum is fitted (dashed line) with an empirical function given by Eq. 1.

The three sets of $(A_i, \alpha_i, B_i, \beta_i)$ values obtained from the fit are $(4.06712 \times 10^{+4}, 3.03 \times 10^{-1}, 2.27 \times 10^{-3}, 6.14 \times 10^{-1})$; $(7.77445 \times 10^{+4}, -3.07 \times 10^{-1}, 1.30 \times 10^{-2}, 5.67 \times 10^{-1})$; $(1.45930 \times 10^{+3}, 1.75, 4.84 \times 10^{-5}, 1.68 \times 10^{-1})$ respectively for three energy ranges. We used this function to generate the neutrons for subsequent generation of CRAND protons described in the next Sec. 2.2.

It might be worth to mention here that actually the energy and directional distribution of the secondary neutrons may depend on the location (with geomagnetic latitude through rigidity cut-off and also to some extent due to atmospheric distribution). So, to achieve a more realistic neutron generation model in this phase of the simulation, one might incorporate the location dependent energy and directional distribution. In the current simulation, for the sake of simplicity, we adopted the averaged distribution in energy and direction over the whole area. However, we confirmed that at different geomagnetic latitude the shape of the energy spectra remains more or less identical. The variation in amplitude of the omnidirectional energy spectrum is taken care by the location dependent particle distribution shown in Fig. 1. We also observed only a nominal deviation in θ_Z distribution at the equatorial region ($0-30^\circ$ geomag-

netic latitude) with respect to the average plot shown in Fig. 2a. We estimated about 20% lower relative flux at the higher θ_Z (or lower $\cos\theta_Z$, i.e., away from zenith) end in this comparison.

2.2. Protons from albedo neutron decay

To generate the protons from the CRAND source, we used the spatial, directional and spectral distribution of albedo neutrons shown in Fig. 1, 2 and 3. At first we generated random neutrons according to these distributions on a spherical surface at 100 km above Earth’s surface. Then protons were generated according to free neutron β -decay scheme. We randomly sampled the neutron decay time (t_D) for each neutron from the decay time distribution function: $\frac{t_D}{\tau_n} \exp\left(-\frac{t_D}{\tau_n}\right)$, where, $\tau_n = 881.5$ s is the neutron mean life time. Then we calculated the position of generation of the proton from the distance travelled by the neutron before its decay as: $v_n \gamma t_D$, where, v_n is neutron velocity (calculated from the kinetic energy and track direction) and γ is the relativistic time dilation factor. For the sake of simplicity, we preserved the direction and kinetic energy of the protons same as the neutrons. In the original simulation calculation we considered all the protons generated inside the magneto-pause ($10 R_E$) boundary. However, considering our current purpose of calculating trapped protons and comparing with *PAMELA* measurement (Adriani et al., 2015), we enforced two conditions limited by the measurement – take account of only those protons which: (i) have kinetic energies in the range of 50 MeV to 4 GeV and (ii) are generated below $2 R_E$. The first limit is obvious due to the energy threshold of the instrument and maximum energy of the trapped particles found by the measurement. The second limit imposed here considering the fact that *PAMELA* can observe the stably trapped protons only for L-shell values in between $\sim 1.18 R_E$ up to $\sim 1.7 R_E$ (Adriani et al., 2015).

2.3. Proton transportation in the geomagnetic field

The trajectory of the protons produced from the decay of neutrons are guided by the geomagnetic field according to their momentum and position. These particles will then be trapped in the magnetic field or deflected (into the outer space

or towards Earth) depending on the mentioned parameters and their tracks can be traced using numerical calculations (Smart & Shea, 2000, 2005).

However, the calculation of the actual charged particle tracks due to its Newton-Lorentz motion in the magnetic field can be computationally expensive. So, instead, we considered the guiding center motion of the particles, while the directional information of the original track is preserved by the pitch angle information. An offhand calculation (with 1000 proton tracks of 50 MeV energy) shows a reduction of the tracking time to $\sim 37\%$.

The equations of motion of the guiding center are given by (Öztürk, 2012):

$$\frac{d\mathbf{R}}{dt} = \frac{\gamma m v^2}{2qB^2} \left(1 + \frac{v_{\parallel}^2}{v^2} \right) \hat{\mathbf{b}} \times \nabla B + v_{\parallel} \hat{\mathbf{b}}, \quad (2)$$

$$\frac{dv_{\parallel}}{dt} = -\frac{\mu}{\gamma^2 m} \hat{\mathbf{b}} \cdot \nabla B. \quad (3)$$

Here \mathbf{R} is the guiding center position of the particle track, which moves in the local magnetic field with magnitude B and directional unit vector $\hat{\mathbf{b}}$. m , q , γ , v and v_{\parallel} are the particle (proton) mass, charge, Lorentz factor, speed and component of velocity parallel to the magnetic field direction respectively. $\mu = \frac{\gamma^2 m v_{\perp}^2}{2B}$ (with v_{\perp} the perpendicular component of the particle velocity), is the magnetic moment of the current generated by the circular motion of the charged particle in the magnetic field.

We calculated the guiding center trajectories of the particle motion in the geomagnetic field by integrating the Equations 2 and 3. We considered the adaptive integration technique using *boost::numeric::odeint* library (Boost C++ libraries, 2020) with *Cash-Karp* algorithm (*runge_kutta_cash_karp54*) for stepper. The initial values supplied to the integration method are: the position of the generated proton from the neutron decay, the velocity component of the particle parallel to the magnetic field and initial stepping time depending on the particle velocity to travel 500 km distance along the guiding center.

However, we record only the stably-trapped particle trajectories satisfying the conditions that, while drifting through the full rotation around the Earth

(360° change of azimuthal angle of the trajectory; we are using geocentric coordinate system) it does not reach: (i) within 40 km from Earth's surface (absorbing atmospheric limit) and (ii) the magnetopause limit at $10 R_E$. Both of these two conditions corresponds to the quasi-trapped or un-trapped particles and are not considered in the present work.

The termination of the stably-trapped trajectory integration depends on the morphology of the drift trajectory. Keeping in mind, the latitude/longitude grid resolution of the order of a degree, during the spatial analysis of the trajectory data, we intend to keep an azimuthal distance of $\sim 1^\circ$ between two successive crossing points of the trajectory with the latitude (say at magnetic-equator). Then, we calculate the number of full drifted rotation of the trajectory required to cross the equator at least 360 times. So the trajectories with higher drift speed (with larger separation between successive crossings) are traced for longer time. This is done for better interpolation of the particle location on the drift shell. The overall information of each trajectory is saved for the analysis purpose described in the next section.

We simulated a total of 10^6 events in which protons generated from the neutron decay are trapped in the geomagnetic field, satisfying the aforementioned trapping conditions. To get this number of trapped particles, the simulation discarded another 2793176 events which did not satisfied the the trapping conditions and correspond to quasi-trapped or untrapped particles and not been considered further.

3. Data Analysis and Results

3.1. Physical parameters

At first, we check the three most important parameters at the generation point of the proton trajectories: position of generation, direction of propagation and kinetic energy of the particle — to look into the facts of delay in neutron decay, coupling of the proton with the geomagnetic field and energetics of the particle distribution. The initial position distribution of the trapped protons

is shown in Fig. 4a, which shows the distance of proton generation from the Earth's center (in this simulation we considered this distance only up to $2 R_E$). It is evident from this figure that the number of CRAND generated protons are increasing beyond $2 R_E$, but, as we have already mentioned earlier, this limit is imposed in the prospect of comparing the results with *PAMELA* measurement. We show the overall distribution of the initial pitch angle (α_i ; i.e., at the position of the proton generation) and the equatorial pitch angle (α_0) of the trapped protons in Fig. 4b. The α_0 values are calculated directly from the magnetic field information of the trajectory at the mirror points (B_m) and magnetic equator (B_0) as $\alpha_0 = \sin^{-1} \sqrt{\frac{B_0}{B_m}}$, averaged over the whole drift trajectory. The higher population near lower pitch angle (i.e., higher probability of particles having velocity nearly along or opposite to the magnetic field lines) can be explained from the following facts. The neutrons are generated in majority near the polar regions (where the inclination of the field lines are larger), as evident from Fig. 1. In addition, more particles are directed towards the zenith as suggested by the distribution of the momentum directions (Fig. 2). However, the scarcity of the protons with extremely low values of initial pitch angle (parallel or anti-parallel to the magnetic field) is due to the effects both from position distribution of the neutron generation and simulation artifact arose from primary particle generation surface and atmospheric distribution consideration as mentioned in Sec. 2.1.

In Fig. 5a, we show the trapped proton distribution with respect to the kinetic energy and the distance of its generation. The overall energy spectrum is shown In Fig. 5b. While the total entrapment efficiency of the CRAND protons in the considered energy range and altitude limit can be estimated from total number of simulated neutrons and entrapped protons given in Sec. 2.3 which is about 26%, a relative calculation of the energy dependent entrapment efficiency was also done. This shows about 40% lesser trapping efficiency at the lower energy end in comparison to that at the higher end and the efficiency increases almost monotonically towards the higher energy end.

We verified the trapped proton trajectories to fulfill the adiabatic conditions,

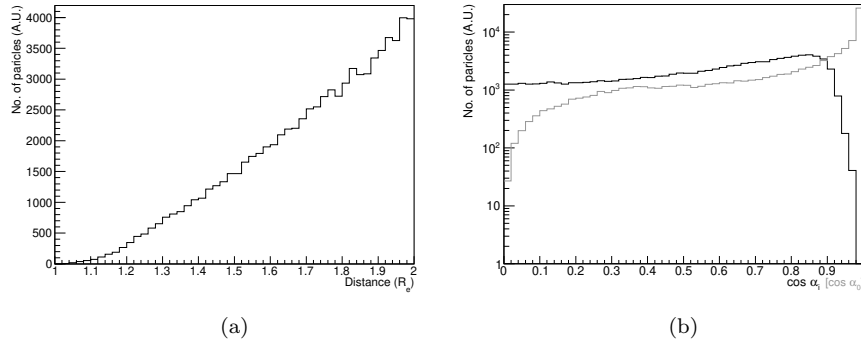


Figure 4: (a) Trapped proton distribution as a function of the distance of initial position of the trajectories. (b) Trapped proton distribution as the function of cosine of the initial pitch angle (black) and the equatorial pitch angle (gray).

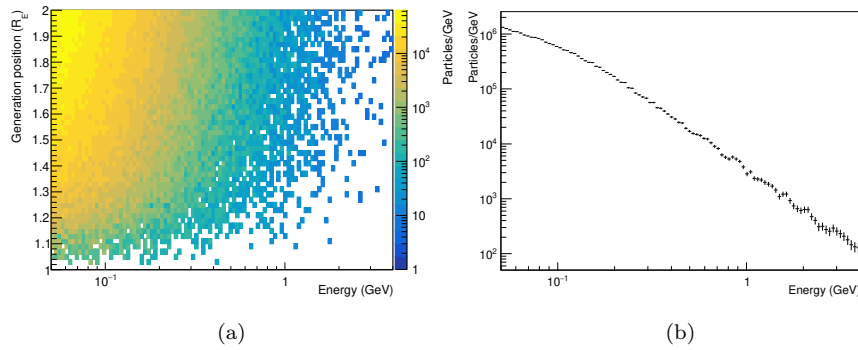


Figure 5: (a) Trapped proton distribution as the function of kinetic energy and distance of initial position of the trajectory. (b) Integrated flux distribution of the trapped protons.

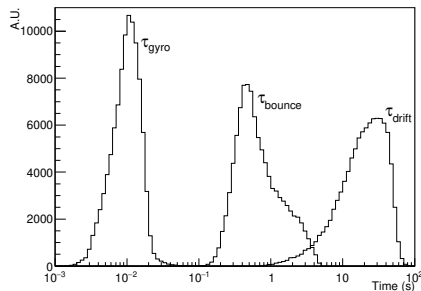


Figure 6: Distribution of temporal scales for three types of motions of all the simulated trapped protons under the effect of geomagnetic field.

particularly checking the hierarchy of the temporal scales:

$$\tau_{gyro} \ll \tau_{bounce} \ll \tau_{drift}, \quad (4)$$

where τ_{gyro} , τ_{bounce} and τ_{drift} are time scales associated to gyration, bounce and drift motions, respectively. τ_{gyro} ($= \frac{2\pi m_p}{qB}$; where m_p proton mass, q charge, B local magnetic field) is calculated from the magnetic field value at the initial position of the proton trajectory. While, τ_{bounce} and τ_{drift} are calculated by averaging the bounce periods and drift periods respectively, over the whole trajectory, obtained from the simulated trajectory information. Figure 6 shows the τ_{gyro} , τ_{bounce} and τ_{drift} distribution for all the simulated trajectories.

3.2. Adiabatic invariants

Here, in this work, we have not considered the gradual energy loss, nuclear scattering or radial diffusion of the trapped particles. So the adiabatic invariants of the trapped particles are conserved. The versions of the adiabatic invariants considered are as follows (Roederer, 1970):

$$M = \frac{\gamma^2 m v_{\perp}^2}{2B}, \quad (5)$$

$$K = \int_{s_m}^{s'_m} (B_m - B(s))^{1/2} ds, \quad (6)$$

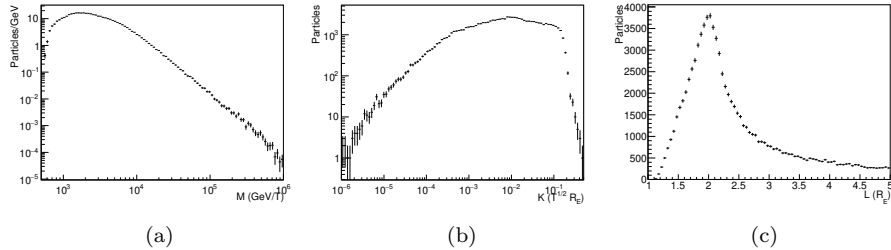


Figure 7: Distribution of adiabatic invariants (a) M , (b) K and (c) L values for all the simulated trajectories.

$$L = \frac{2\pi\mu_E}{R_E\Phi}. \quad (7)$$

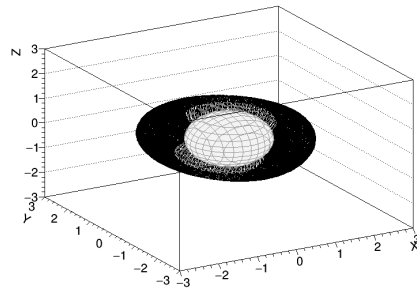
The first invariant M is calculated using the particle velocity and magnetic field value at the initial position of the track. The second invariant K is calculated by integrating the magnetic field along the guiding center path between two successive mirror points. The average K value over the whole trajectory has been used as the second invariant of the trajectory. We consider L value as the third invariant. It is directly calculated from distance of the trajectory from the Earth's center at the geomagnetic equator, where the track is at the highest position. We subsequently calculate Φ , the magnetic flux inside the drift shell from Eq. 7, where R_E is Earth's radius and μ_E Earth's magnetic dipole moment (arbitrarily taken for 2008 A.D. to compare with the results from *PAMELA* measurements).

The distribution of the three adiabatic invariants, for all the simulated particles are shown in Fig. 7. The drop in population at extreme low M values may be attributed to the scarcity of trapped particles at the lowest values of initial pitch angle as shown in Fig. 4b. The cut-offs apparent in the K plot at around $10^{-1} T^{1/2} R_E$ and in L plot at $2 R_E$ are due to the limit used in the simulation for the particle generation distance. However, we calculated the trapped particle trajectories beyond this distance (up to the average magnetopause distance at $10 R_E$).

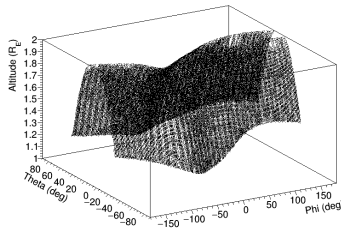
3.3. Spatial distribution of trapped protons

A stably trapped particle track creates a drift shell surrounding the Earth and can be detected from any position in the continuous shell given a sufficiently long entrapment time. So, from the simulation point-of-view, we can spatially distribute one event to contribute all over the positions throughout the drift shell, improving the particle statistics without using extra computational resource for simulating more events. However, we must interpolate the trajectory to represent the drift shell. In Fig. 8a, we show, for example, the guiding center trajectory of a 288.7 MeV proton trapped in the geomagnetic field started from a position at $1.66 R_E$ altitude and with initial pitch angle 135.9° . The trajectory chosen here arbitrarily just to present the analysis procedure. For the analysis purpose, we replotted the trajectory in the geocentric coordinate system (ϕ , θ and elevation from Earth's center), with $1^\circ \times 1^\circ$ grid in ϕ/θ and dividing the elevation range of 1–2 R_E in 320 bins (giving $\Delta Alt \sim 20$ km). The trajectory plot is shown in Fig. 8b which represents the drift shell for the corresponding track. Then we can calculate the distribution of the drift shell interceptions at each layer of different elevation (measurement altitude) and interpolate the interception locations. This is shown in Fig. 8c, for example at the measurement surface at $1.7 R_E$. We adopted this method to ensure that, for the simulated trajectories, where the azimuthal gap between two subsequent bouncing tracks are larger (than the considered phi grid, i.e., 1° here), we don't have to rotate the trajectory around Earth for too many times, which can be computationally expensive. Instead, we fill the gaps (between subsequent locations of track interceptions) by interpolation as shown in Fig. 8c.

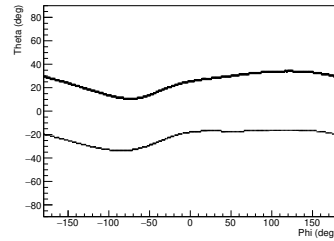
Then we calculate the overall contribution of all the simulated trapped trajectories at different measurement altitudes. In Fig. 9, for example, we show the spatial distribution of proton trajectories integrated over four different altitude ranges at LEO: 300–385, 385–470, 470–555 and 555–640 km. It is evident from these plots that the high energy trapped protons in the considered energy range and with all pitch angles are largely concentrated at north-east of the geographic south pole below the African peninsula.



(a)



(b)



(c)

Figure 8: (a) Example of a trapped particle track (guiding center) for a 288.7 MeV proton started at $1.66 R_E$ with initial pitch angle 135.9° . (b) Same track represented in the grid view of geocentric coordinate system. (c) Distribution of the drift shell interception locations with a spherical surface at $1.7 R_E$.

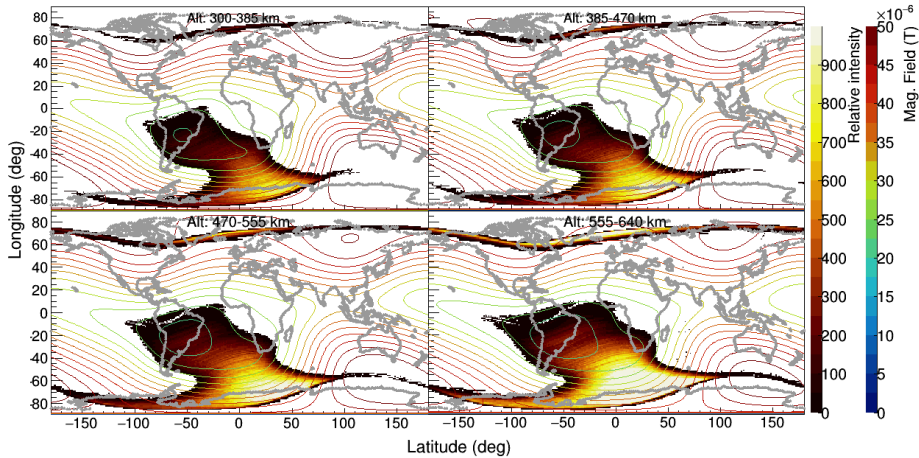


Figure 9: Distribution of trapped proton trajectories from CRAND in geographical latitude/longitude at four different altitude ranges. Geomagnetic field contours at the corresponding heights has been drawn overlaid on the proton distribution plots.

3.4. Flux normalization

The trapped proton intensity at some fixed location (on a satellite orbit) and at a given time (of measurement) can be expressed as a function of kinetic energy (E) and time, in the following form (Selesnick, 2001):

$$j(E, t) = v \int_{t_0}^t S(E', t') \exp\left(-\int_{t'}^t \left(\frac{\partial}{\partial E''} \frac{dE}{dt} + \frac{1}{\tau}\right) dt'\right), \quad (8)$$

where v is the speed of the particle corresponding to the kinetic energy, S is the source rate, τ is the trapping lifetime and $\frac{dE}{dt}$ represents the continuous energy change of the particle. At the initial time $t = t_0$, $j = 0$, when E corresponds to maximum energy of the trapped proton. However, in this work, we consider crude approximation of no gradual energy loss (through ionization; to free electrons or adiabatic energy change caused by secular geomagnetic variation) and no trapped particle loss through nuclear scattering or due to the effect from geomagnetic storms. So, $\frac{dE}{dt} = 0$ and $\tau = \infty$; we only have the time integration over the source term, which, in this present case, is the GCR contribution through CRAND mechanism. This approximation has severe implication over the absolute flux calculation of the trapped particles but reveals the relative

flux distribution anyway.

The normalization factor of the simulation events to calculate the trapped proton flux can be given by:

$$NF = \frac{\int_{T_s} \int_{A_s} \int_{\Omega_s} \int_{E_s} \frac{dN}{dE} dE d\Omega da dt}{N_{sim} \int_{A_m} \int_{\Omega_m} d\Omega da}, \quad (9)$$

where $\frac{dN}{dE}$ is the source function of the albedo neutron energy spectrum given by Eq. 1 and N_{sim} ($= 10^6$) is the total number of simulated events giving trapped particles. Integration of the source function is done over the energy range $E_s = [50 \text{ MeV}, 4 \text{ GeV}]$, over 2π solid angle (Ω_s) and over the area (A_s) of albedo neutron generation surface (spherical surface at 100 km from Earth's surface). Integration for the part at the denominator, corresponds to the measurement of the trapped protons and is carried over 4π solid angle (Ω_m) and over the spherical surface area A_m at the measurement altitude ($\sim 500 \text{ km}$) considering the average *PAMELA* orbit. The time limit T_s , which indicates the accumulation time of the trapped particles, is undefined here. Since, we are not considering the loss of the trapped particles, the average value of T_s can only be inferred using the information of the measured flux. In this calculation, considering a gross comparison with the *PAMELA* measurement of the trapped proton flux, we get $T_s \sim 0.1$ year. This value is somewhat lower in comparison to the trapped proton residence time range mentioned in Selesnick et al. (2007) as less than a year to ~ 4000 years. But this can be justified for the high energy particles (with smaller drift time scale) we are considering here and since we are ignoring the particle loss effects.

4. Comparison with PAMELA Measurements

We compare the simulation results with the measurement of trapped proton fluxes at LEO by the *PAMELA* experiment (Adriani et al., 2015). *PAMELA* measured the trapped proton fluxes at $350 \div 610 \text{ km}$ altitude between July, 2006 and September 2009. The proton trajectories were reconstructed using tracing programs based on numerical integration method (Smart & Shea, 2000, 2005)

to select the stably trapped trajectories used for the analysis. A total of 7.3×10^6 stably trapped particles were sampled for the analysis out of total 9×10^6 detected events (including quasi- and un-trapped trajectories). We considered similar order of event number in the current simulation to get comparable statistics in the results.

In Fig. 10, we show the distribution of trapped proton flux integrated over the pitch-angle range covered by *PAMELA*, at different altitudes and energy ranges. We refer to the Fig. 1 of Adriani et al. (2015) for the comparison of the distribution. We rebinned the θ/ϕ distribution in $2^\circ \times 2^\circ$ grid for the comparison. We also added an uncertainty of $\sigma = 3^\circ$ to the simulated track positions (in θ/ϕ), to account the uncertainty in payload orientation measurement and angular resolution of the detector. We sampled the detector location over all the region at different altitude (but limited by the satellite orbit inclination of 70°) and obtained the trajectories within the acceptance angle of the detector, by calculating the angle between the detector direction (towards the local zenith) and trajectory direction (obtained from the local pitch angle of the trajectory) at the location of the detector. However, this approach averages the calculation over the gyro-phase angle and neglects the east-west effect due to atmospheric absorption at larger gyro-radius. The simulated result of the trapped proton distribution map precisely reproduces the measured distribution by *PAMELA* which is concentrated around the South Atlantic Anomaly (SAA) region. Relation of the area coverage with the altitude and energy range is also apparent from the plot. In particular, the feature reported in Adriani et al. (2015), that the proton flux is more concentrated in the southeast part of SAA is also apparent here. To make this feature more apparent we also indicate the peak points of the distribution on the same plot. The explanation of the peaks shifted towards the southeast can be visible from Fig. 9, which shows that the trapped protons, irrespective of *PAMELA* acceptance angle, are concentrated near the south-polar region below the African peninsula. We have already mentioned in Sec. 3.4, the absolute value of the integral flux depends on the accumulation time of the trapped particles, which require to include the loss effects to calcu-

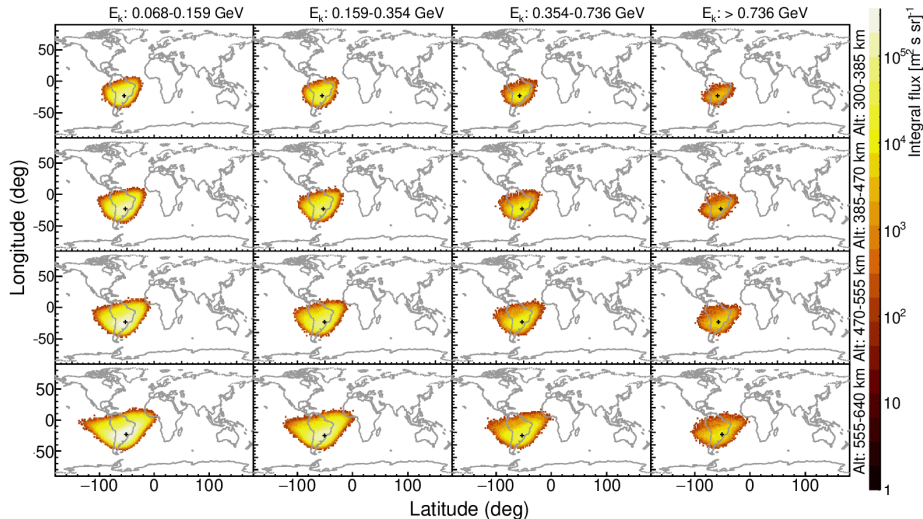


Figure 10: Simulated trapped proton integral flux distribution, integrated over the pitch angle range covered by *PAMELA*, in geographical coordinates, at different altitudes (rows) and energy ranges (columns). The peak of the distributions are indicated by the plus signs.

late it. Since, in this work we did not consider the loss effects, to present the integral flux we simply scaled the value by varying the T_s value to grossly match the *PAMELA* measurement.

For additional comparison with the measured data, we also plot the integral proton flux with other parameters than spatial distribution. Figure 11a shows the proton integral fluxes as a function of second and third adiabatic invariants (K and Φ), for the particles in *PAMELA* field of view, at different kinetic energy ranges. We plotted the result in $K^{1/2}$ and $\log_{10} \Phi$ coordinates for better resolution (and for the sake of direct comparison with *PAMELA* results). Figure 11b shows the same fluxes as a function of equatorial pitch angle and L value. These results can be compared with the results from the *PAMELA* measurements shown in Fig. 2 and 3 of Adriani et al. (2015). While the overall distribution agrees well with the observed data, the comparisons show some differences in the extent of the energy dependent data patches in K and α_0 . These differences can be attributed, as discussed in Adriani et al. (2015), to the spacecraft orbit which constraint the observation of the equatorial mirror-

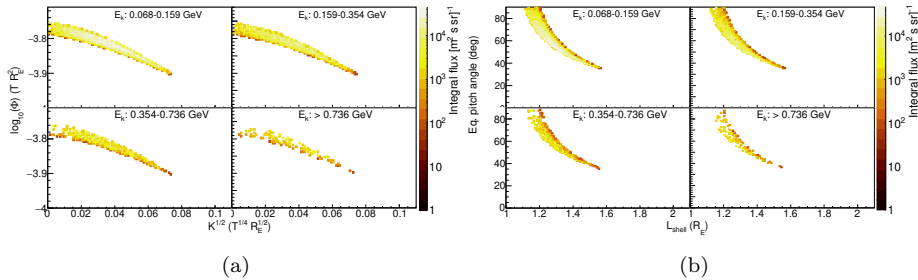


Figure 11: (a) Proton integral fluxes as a function of K and Φ at different kinetic energy bins in the pitch angle range covered by *PAMELA*. (b) The similar distribution as a function of L-shell parameter and equatorial pitch angle.

ing protons only for L values up to $\sim 1.18 R_E$. However, one thing should be mentioned regarding the simulation aspect — here in this work we optimized the algorithm to gain statistically in the spatial distribution of the trapped particles where one trajectory can contribute to the entire drift shell region. But, since this optimization has no effect on increasing the number of trajectories, the analysis concerning the parameters attributed to a trajectory has little gain from the algorithm. We need to simulate more particles for a better comparison of these aspects shown in Fig. 11.

5. Conclusions

We conducted a thorough simulation to calculate the trapped proton radiation contribution at LEO, through the CRAND mechanism. This is the principal contributor to the proton radiation at this region for proton energy $\gtrsim 50$ MeV. For this purpose we developed a simulation framework to calculate the secondary particles from the atmospheric interaction of the GCRs. The protons, produced from the β -decay of the albedo neutrons from these GCR interactions, are then geomagnetically trapped and their trajectories have been calculated using the guiding center equation of the particles. We studied the spatial as well as the phase-space distribution of the trapped protons and compared the results with the observation by *PAMELA* mission, giving satisfactory

agreement. This study also helps to understand certain features of the measured flux distribution. However, in this calculation we considered only the source term, neglecting the loss of trapped particles over time, due to various scattering and energy loss processes. Consideration of the loss term is important for the complete understanding of the radiation distribution and will be added in the future extension of the work.

While, in this work we have particularly concentrated on the trapped proton distribution at LEO and to compare the results with *PAMELA* measurement, the same simulation framework can be used, to study the overall inner radiation belt by investigating the spatial distribution, trapping limits etc. We can also consider the contributions from other sources to the radiation belt like solar proton events with some modification to the source particle generation and the results can be compared to the recent empirical models like AP9 (Ginet et al., 2013) and that given by Selesnick et al. (2007).

The simulated result agrees well with the observation which is evident from Fig. 10. This flux distribution is mainly due to the trapped trajectories with L values less than 1.6. However, a closer inspection of the overall flux distribution shown in Fig. 9 reveals that there are two different populations of trajectories that comprise the distribution. The stably trapped particles with $L < 2$ are visible near the SAA region. Trajectories in the other part comprising the horns and deposition near the south pole mainly show higher L values whose entrapment are theoretically perplexed for such high energy particles. The origin and nature of these “trapped” trajectories could be better revealed by a more detailed investigation of the morphology of these trajectories which has not been done yet in this work and is pending for the future extension of this work.

6. Acknowledgments

We express our sincere gratitude to M. Boezio (INFN, Trieste) and A. Bruno (NASA/GSFC) for the helpful discussions. This work has been done under partial financial support from the Science and Engineering Research Board

(SERB, Department of Science and Technology, Government of India) project no. EMR/2016/003870. We also thank the Higher Education department of West Bengal, for a Grant-In-Aid which allowed us to carry out the research activities at ICSP.

References

- Adriani, O., Barbarino, G. C., Bazilevskaya, G. A. et al. (2015). Trapped proton fluxes at low Earth orbits measured by the PAMELA experiment. *Astrophys. J. Lett.*, *799:L4*, 7–14. doi:10.1088/2041-8205/799/1/L4.
- Agostinelli, S., Allison, J., Amako, K. et al. (2003). Geant4 - a simulation toolkit. *Nucl. Instrum. Methods Phys. Res., Sect. A*, *506/3*, 250–303. doi:10.1016/S0168-9002(03)01368-8.
- Boost C++ libraries (2020). https://www.boost.org/doc/libs/1_66_0/libs/numeric/odeint/doc/html/index.html. Accessed: 10 February 2020.
- Farley, T. A., & Walt, M. (1971). Source and loss processes of protons of the inner radiation belt. *J. Geophys. Res.*, *76*, 8223–8240. doi:10.1029/JA076i034p08223.
- Getselev, I. V., Gusev, A. N., Darchieva, L. A. et al. (1991). Model of spatial-energetic distribution of charged particles (protons and electrons) fluxes in the Earth’s radiation belts. *INP MSU Preprint, MGU-91-37/241*.
- Ginet, G. P., O’Brien, T. P., Huston, S. L., Johnston, W. R., Guild, T. B., Friedel, R., Lindstrom, C. D., Roth, C. J., Whelan, P., Quinn, R. A., Madden, D., Morley, S., & Su, Y.-J. (2013). AE9, AP9 and SPM: New Models for Specifying the Trapped Energetic Particle and Space Plasma Environment. *Space Sci. Rev.*, *179*, 579–615. doi:10.1007/s11214-013-9964-y.
- Gussenhoven, E. G., M. S.; Mullen (1993). Space Radiation Effects Program - An overview. *IEEE Trans. Nucl. Sci.*, *40/2*, 221–227. doi:10.1109/23.212345.

- Heynderickx, D., Kruglanski, M., Pierrard, V. et al. (1999). A low altitude trapped proton model for solar minimum conditions based on SAMPEX/PET data. *IEEE Trans. Nucl. Sci.*, *46*, 1475–1480. doi:10.1109/23.819110.
- Hudson, M. K., Kress, B. T., Mazur, J. E. et al. (2004). 3D modeling of shock-induced trapping of solar energetic particles in the Earth’s magnetosphere. *J. Atmos. Sol. Terr. Phys.*, *66*, 1389–1397. doi:10.1016/j.jastp.2004.03.024.
- Huston, S. L., Kuck, G. A., & Pfitzer, K. A. (1996). Low Altitude Trapped Radiation Model Using TIROS/NOAA Data. In J. F. Lemaire, D. Heynderickx, & D. N. Baker (Eds.), *Radiation Belts: Models and Standards* (p. 119). Washington, DC USA: American Geophysical Union.
- Looper, M. D., Blake, J. B., Cummings, J. R. et al. (1996). SAMPEX observations of energetic hydrogen isotopes in the inner zone. *Radiat. Meas.*, *26/6*, 967–978. doi:10.1016/S1350-4487(96)00098-4.
- Lorentzen, K. R., Mazur, J. E., Looper, M. D. et al. (2002). Multisatellite observations of MeV ion injections during storms. *J. Geophys. Res. A: Space Phys.*, *107(A9)*, 1231. doi:10.1029/2001JA000276.
- Öztürk, M. K. (2012). Trajectories of charged particles trapped in the Earth’s magnetic field. *Am. J. Phys.*, *80 (5)*, 420–428. doi:10.1119/1.3684537.
- Picone, J. M., Hedin, A. E., Drob, D. P., & Aikin, A. C. (2002). NRL-MSISE-00 Empirical Model of the Atmosphere: Statistical Comparisons and Scientific Issues. *J. Geophys. Res. A: Space Phys.*, *107*, 1468. doi:10.1029/2002JA009430.
- Picozza, P., Galper, A. M., Castellini, G. et al. (2007). PAMELA: A payload for antimatter matter exploration and light-nuclei astrophysics. *Astropart. Phys.*, *27/4*, 296–315. doi:10.1016/j.astropartphys.2006.12.002.
- Roederer, J. G. (1970). *Dynamics of geomagnetically trapped radiation*. Springer-Verlag New York Heidelberg Berlin. doi:10.1007/978-3-642-49300-3.

- Sarkar, R., Roy, A., & Chakrabarti, S. K. (2020). Simulation of cosmic rays in the Earth's atmosphere and interpretation of observed counts in an X-ray detector at balloon altitude near tropical region. *Adv. Space Res.*, *65*, 189–197. doi:10.1016/j.asr.2019.09.046.
- Sawyer, D. M., & Vette, J. I. (1976). AP-8 trapped proton environment for solar maximum and solar minimum. *NASA Tech. Memo, TM-X-72605*.
- Selesnick, R. S. (2001). Simulation of the anomalous cosmic ray radiation belt with atmospheric production and decay. *Geophys. Res. Lett.*, *28*, 3417–3420. doi:10.1029/2001GL013383.
- Selesnick, R. S., Looper, M. D., & Mewaldt, R. A. (2007). A theoretical model of the inner proton radiation belt. *Space Weather*, *5*, S04003. doi:10.1029/2006SW000275.
- Singer, S. F. (1958). Trapped albedo theory of the radiation belt. *Phys. Rev. Lett.*, *1*, 181–183. doi:10.1103/PhysRevLett.1.181.
- Smart, D. F., & Shea, M. A. (2000). Final Report, Grant NAG5-8009. Center for Space Plasmas and Aeronomic Research, The University of Alabama in Huntsville.
- Smart, D. F., & Shea, M. A. (2005). A review of geomagnetic cutoff rigidities for earth-orbiting spacecraft. *Adv. Space Res.*, *36*, 2012–2020. doi:10.1016/j.asr.2004.09.015.
- Thébault, E., Finley, C., & Toh, H. (2015). Special issue “International Geomagnetic Reference Field: the 12th generation”. *Earth Planets and Space*, *67*, 79–98. doi:10.1186/s40623-015-0313-0.
- Tsyganenko, N. A., & Andreeva, V. A. (2016). An empirical RBF model of the magnetosphere parameterized by interplanetary and ground-based drivers. *J. Geophys. Res. A: Space Phys.*, *121*, 10786–10802. doi:10.1002/2016JA023217.

Vos, E. E., & Potgieter, M. S. (2015). New modeling of galactic proton modulation during the minimum of solar cycle 23/24. *Astrophys. J.*, *815*, 119. doi:10.1088/0004-637X/815/2/119.